

Probing Cosmic Ray Transport with *Radio Synchrotron Harps* in the Galactic Center

TIMON THOMAS,¹ CHRISTOPH PFROMMER,¹ AND TORSTEN ENSSLIN²

¹*Leibniz-Institute for Astrophysics Potsdam (AIP), An der Sternwarte 16, 14482 Potsdam, Germany*

²*Max Planck Institute for Astrophysics, Karl-Schwarzschild-Str. 1, 85741 Garching, Germany*

ABSTRACT

Recent observations with the MeerKAT radio telescope reveal a unique population of faint non-thermal filaments pervading the central molecular zone (CMZ). Some of those filaments are organized into groups of almost parallel filaments, seemingly sorted by their length, so that their morphology resembles a harp with radio emitting “strings”. We argue that the synchrotron emitting GeV electrons of these radio harps have been consecutively injected by the same source (a massive star or pulsar) into spatially intermittent magnetic fiber bundles within a magnetic flux tube or via time-dependent injection events. After escaping from this source, the propagation of cosmic ray (CR) electrons inside a flux tube is governed by the theory of CR transport. We propose to use observations of radio harp filaments to gain insight into the specifics of CR propagation along magnetic fields of which there are two principle modes: CRs could either stream with self-excited magneto-hydrodynamical waves or diffuse along the magnetic field. To disentangle these possibilities, we conduct hydrodynamical simulations of either purely diffusing or streaming CR electrons and compare the resulting brightness distributions to the observed synchrotron profiles of the radio harps. We find compelling evidence that CR streaming is the dominant propagation mode for GeV CRs in one of the radio harps. Observations at higher angular resolution should detect more radio harps and may help to disentangle projection effects of the possibly three-dimensional flux-tube structure of the other radio harps.

Keywords: Galaxy: center — radiation mechanisms: non-thermal — cosmic rays — methods: numerical

1. INTRODUCTION

Radio observations of the Galactic center region show many isolated, elongated filaments (Lang et al. 1999; LaRosa et al. 2001; Nord et al. 2004; Yusef-Zadeh et al. 2004). Recent high-resolution observations with the MeerKAT radio telescope found that the filaments trace bipolar bubbles that are rising from the CMZ near the Galactic center (Heywood et al. 2019). The filaments are characterised by a high aspect ratio, a filament-aligned magnetic field (Lang et al. 1999), strongly polarized emission (LaRosa et al. 2001), and a hard spectral index that steepens away from the geometric center of the filaments (Law et al. 2008). Hence, these non-thermal filaments (NTFs) are illuminated by synchrotron-emitting electrons.

Explanations for injecting relativistic electrons into NTFs include magnetic reconnection (Lesch & Reich 1992; Bicknell & Li 2001), acceleration in young stellar clusters (Yusef-Zadeh 2003), magnetized wakes of molecular clouds (Shore & LaRosa 1999; Dahlburg et al. 2002), pulsar wind nebula (Bykov et al. 2017; Barkov & Lyutikov 2019), stellar winds of massive stars (Rosner & Bodo 1996; Yusef-Zadeh & Wardle 2019), and even annihilation of light dark matter (Linden et al. 2011). Whether the origin of the parsec-sized straight NTFs is causally linked to the electron source that powers them is unclear.

To explain the brightness of NTFs, we need to take a closer look at CR propagation. The Lorentz force ties CRs to any macroscopic magnetic field and causes the CRs to follow the field line motion. When magnetic fields are frozen into and move along with the fluid, CRs are bound to follow these fluid motions. This is called *CR advection* and shown in the right-hand panel of Fig. 1. We expect CR advection to be unimportant for NTFs as their straight morphology excludes

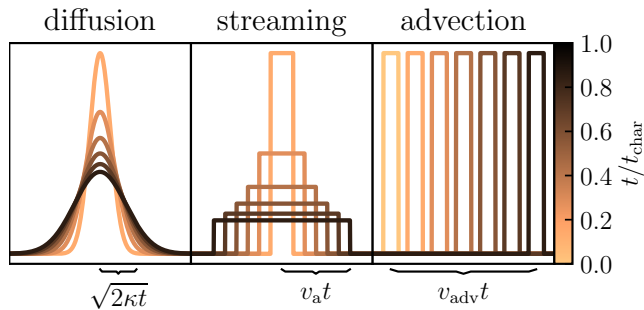


Figure 1. Archetypical transport modes of CR fluids. Left: when CRs are weakly scattered by Alfvén waves, they diffuse away from a given source (after an initial time) with a root-mean-square velocity of $\sqrt{2\kappa/t}$ (where t is the time and κ denotes the diffusion coefficient) along the magnetic field. Middle: if CRs are effectively scattered, they stream with the Alfvén speed, v_a , along the magnetic field. Either one or both of these processes may be realized while CRs are tied to frozen-in magnetic fields, causing them to be advected with the bulk plasma velocity, v_{adv} (right).

large-scale gas motions perpendicular to the NTFs that change their appearance.

Of particular interest for NTFs is CR propagation along the mean magnetic field. It can be classified into two principle modes depending on the frequency of particle scatterings with magneto-hydrodynamic waves. (i) If these scatterings are frequent, then the ensemble average of the particle distribution follows the motions of their non-relativistic scattering centers while individual particles move with their relativistic velocities. This is the basis for describing CRs as a hydrodynamical fluid on scales larger than the effective mean-free path. (ii) If CR-wave scatterings are infrequent, CRs move ballistically and a kinetic description of individual particle trajectories is appropriate. Malkov (2017) showed that CRs leave the ballistic regime after three characteristic scattering times and enter a diffusive, fluid-like behaviour (left panel of Fig. 1).

For CRs with energies below ~ 200 GeV, magneto-hydrodynamical (MHD) waves are believed to be the dominant source of scattering (Yan & Lazarian 2011; Blasi et al. 2012). CRs can provide their own scattering centers by exciting Alfvén waves on scales comparable to their gyroradii through the gyroresonant instability (Kulsrud & Pearce 1969). These Alfvén waves interact with CRs so that the effective CR drift velocity approaches the Alfvén velocity, v_a , which is referred to as *CR streaming*.

CRs injected by a compact source excite Alfvén waves while leaving their acceleration site. These Alfvén waves are travelling in opposite directions along the magnetic field away from the source. Both leading fronts of Alfvén

waves span an expanding region populated by CRs. Due to their confinement into this region, the CR population rarefies. Assuming perfect confinement, there is a sharp transition between locations that are occupied by or free of injected CRs (see middle panel of Fig. 1).

This fundamental difference between CR streaming and diffusion allows us to differentiate between the two modes by studying the radio synchrotron brightness along NTFs: (i) the synchrotron emission from diffusing CR electrons smoothly fades away from a compact source while streaming CR electron populations show a central constant brightness level and a sharp transition to any background emission and (ii) as indicated in Fig. 1, the root-mean-square distance of diffusing CR electrons increases as $\sqrt{2\kappa t}$ while in the CR streaming model, it increases linearly with time as $v_a t$. If we were to observe equidistantly-spaced snapshots of the two propagation modes, then the envelope of the snapshots should either show a bell shape (for CR diffusion), a triangle (for pure CR streaming), or an inverse bell shape (for CR streaming + diffusion).

In this Letter we are studying a particular class of NTFs that we call *radio synchrotron harps* and of which we show two examples in Fig. 2. We will argue that those objects provide a rich avenue to study CR transport and propagation using radio observations.

2. SOURCES POWERING NON-THERMAL FILAMENTS

A massive star or pulsar moving through the CMZ with velocity $v_* \sim v_a$ can intersect and inject CRs into a magnetic flux tube that has been stretched by the bipolar outflow from the CMZ (Heywood et al. 2019). We conjecture that the perpendicular radio harp sizes correspond to the radial flux-tube extents while the regular arrangement of the harp “strings” in Fig. 2 either represents intermittent magnetic fiber bundles within a magnetic flux tube or are a signature of time-dependent injection of CRs into the more homogeneous magnetic flux tube. In the latter case, the intermittency of the radio “strings” might reveal details of the magnetic reconnection process around the wind termination shock that enables CRs to escape. In both cases, the different “string” lengths show a chronological sequence of CR injection events onto an NTF. After injection, the CRs propagate along the magnetic filament, which decreases their energy density and increases their spatial extent. Hence, NTFs with more recently injected CRs appear shorter and brighter while previously injected CRs form longer and fainter filaments. The resulting morphology is that of a filamentary isosceles triangle (or bell) with a bright apex and a fainter base, see Fig. 2.

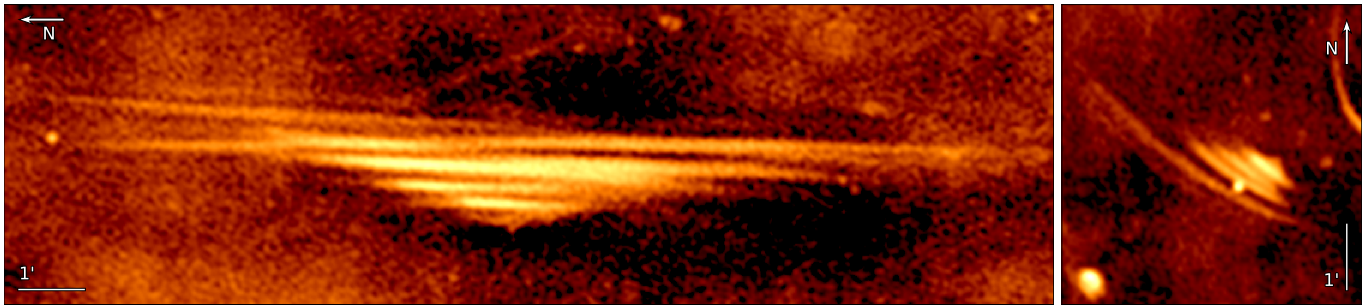


Figure 2. Two radio harps in the MeerKat observation of the CMZ (Heywood et al. 2019). Left: the NTF G359.85+0.39 was discovered by LaRosa et al. (2001); also named N10 in Law et al. (2008). Right: G359.47+0.12 was first imaged by Heywood et al. (2019). Their names correspond to their position in Galactic coordinates.

Wind termination shocks of massive stars—Electrons generated at wind termination shocks or bow shocks of massive stars can illuminate NTFs (Rosner & Bodo 1996; Yusef-Zadeh & Wardle 2019). Massive stellar winds interact with their local interstellar medium (ISM) by building up an interaction layer between the wind interior and the ISM. This layer is confined by a bow shock that encompasses the shocked ISM and a wind termination shock. These shocked fluids are initially separated by a contact discontinuity, which becomes unstable due to Rayleigh-Taylor instabilities that cause mixing of both fluids. At both shocks, low-energy electrons can be accelerated to relativistic energies via diffusive shock acceleration (e.g., del Valle & Pohl 2018). Some bow shock complexes are luminous enough for observable synchrotron emission (Benaglia et al. 2010, for the bow shock of a runaway O star). The stand-off radius R between star and bow shock is given by the pressure balance between stellar wind and ISM:

$$R = \left(\frac{\dot{M}v_\infty}{4\pi(\rho_{\text{ISM}}v_\star^2 + P_{\text{ISM}} + B^2/8\pi)} \right)^{1/2} \sim 0.05 \text{ pc}, \quad (1)$$

where $\dot{M} \sim (10^{-8} - 10^{-5})M_\odot \text{ yr}^{-1}$ is the mass loss rate, $v_\infty \sim (1000 - 2500) \text{ km s}^{-1}$ is the terminal wind velocity, $v_\star \sim \text{few} \times 10 \text{ km s}^{-1}$ is the relative velocity of the star, ρ_{ISM} and P_{ISM} are the ambient ISM density and pressure, and B is the ISM magnetic field strength. We assume that the NTFs are embedded in the warm CMZ phase with gas temperature $T = 10^4 \text{ K}$ and number density $n = 100 \text{ cm}^{-3}$. This implies magnetically dominating NTFs with $B \sim 200 \mu\text{G}$ and a plasma beta $\beta = P_{\text{ISM}}/(B^2/8\pi) = 2c_s/v_a \sim 0.1$, which explains the straight NTF morphology that is not affected by turbulent gas motions. The total kinetic luminosity of the stellar wind is

$$L_{\text{wind}} = \frac{1}{2}\dot{M}v_\infty^2 \sim 1 \times 10^{35} \text{ erg s}^{-1} \quad (2)$$

so that the wind termination shock is

$$\frac{L_{\text{wind}}}{L_{\text{bow}}} = \frac{\dot{M}v_\infty^2}{\rho_{\text{ISM}}v_\star^3 2\pi R^2} \sim 10^2 \quad (3)$$

times more powerful in comparison to the bow shock, implying that the termination shock dominates the yield of accelerated CRs. Assuming that all kinetic wind energy is dissipated at the wind-termination shock and assuming an electron acceleration efficiency of 0.1%, the total CR electron luminosity is

$$L_e = 1 \times 10^{-3} L_{\text{wind}} \sim 1 \times 10^{32} \text{ erg s}^{-1}. \quad (4)$$

Magnetized winds of rotating stars result in perpendicular termination shocks that can accelerate electrons (Xu et al. 2019) but not protons (Caprioli & Spitkovsky 2014).

While moving through the ISM, the stellar wind bubble piles up a magnetic draping layer at the contact discontinuity. Accelerated electrons diffuse onto these field lines and escape from their acceleration site. Subsequently, they move away from the star, emit synchrotron radiation in the strongly magnetized flux tubes of the ISM, and illuminate the NTFs (see left panel of Fig. 3).

Pulsar winds—Another possible source of CR electrons in the NTFs are pulsar wind nebulae (PWN, Barkov & Lyutikov 2019). PWNs are fueled by a central pulsar that is characterised by its spin-down luminosity $\dot{E} \sim 5 \times 10^{37} \text{ erg s}^{-1}$. The wind is launched at the light cylinder of the pulsar’s magnetosphere, where electron-positron pairs leave the magnetosphere and are accelerated by the strong electromagnetic fields. Further acceleration can take place in reconnection layers of the striped pulsar wind. Similar to a stellar wind, the pulsar wind is separated from the ISM by a layer consisting of the wind termination shock, a contact discontinuity and a possible bow shock. An ISM magnetic field that is draped around the pulsar wind can reconnect at the contact discontinuity with magnetic field originating from the wind interior (Barkov & Lyutikov 2019; Barkov

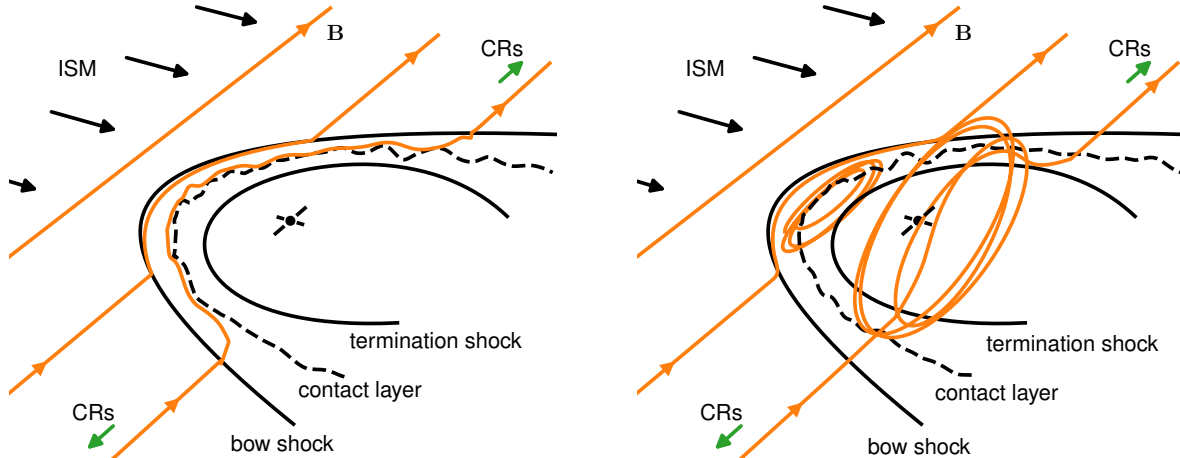


Figure 3. Sketches of possible scenarios that can inject relativistic CRs into NTFs. *Left:* a massive star located in the center drives a stellar wind that builds a wind bubble terminating at a shock. This shock accelerates CRs, which diffuse onto draped ISM magnetic field lines, which experienced mixing with the shocked wind via Rayleigh-Taylor instabilities and escape into the ISM. *Right:* a pulsar drives the wind by accelerating electron-positron pairs towards the wind termination shock. Piled up field lines behind the wind termination shock can reconnect with the ISM magnetic field, allowing CRs to escape. See text for additional discussion.

et al. 2019). This allows relativistic particles to escape from the PWN into the ISM, see the right-hand panel of Fig. 3. The stand-off distance of the pulsar wind is

$$R = \left(\frac{\dot{E}}{4\pi c(\rho_{\text{ISM}}v_{\star}^2 + P_{\text{ISM}} + B^2/8\pi)} \right)^{1/2} \sim 0.05 \text{ pc.} \quad (5)$$

Not all electrons leave the PWN so that the luminosity of NTF-injected electron-positron pairs is estimated to be

$$L_e = 2.5 \times 10^{-4} \frac{\dot{E}}{\sigma} \sim 1 \times 10^{32} \text{ erg s}^{-1}, \quad (6)$$

where $\sigma \sim 100$ is the pulsar wind magnetization.

Radio emission from non-thermal filaments—Both scenarios are comparable in terms of their energy budget and size of the acceleration site. Thus, the energy injected into a flux tube

$$E_{\text{CR}} = f_{\text{esc}} \frac{R}{v_{\star}} L_e \sim 5 \times 10^{42} \text{ erg}, \quad (7)$$

is the same for both sources. Here, $f_{\text{esc}} \sim 0.3 - 1$ is the time fraction during which CRs near the wind termination shock are injected into a flux tube. Furthermore, assuming that the injected electrons/pairs have a Lorentz factor $\gamma \sim 10^3$, they emit synchrotron radiation at

$$\nu = \frac{3eB\gamma^2}{2\pi m_e c} \sim 1.5 \text{ GHz} \quad (8)$$

with a total luminosity of

$$L_{\text{syn}} = E_{\text{CR}} \frac{\sigma_{\text{T}} B^2 \gamma}{6\pi m_e c} \sim 2 \times 10^{29} \text{ erg s}^{-1}, \quad (9)$$

which corresponds to a spectral flux of

$$F_{\text{syn}} = \frac{L_{\text{syn}}}{2\pi d^2 \nu} \sim 2 \text{ mJy} \quad (10)$$

at a distance of $d = 8.2$ kpc. Within the uncertainties, this matches the radio harp flux. The associated synchrotron cooling time of $\sim 10^6$ yr is much longer than the CR propagation time of ~ 60 kyr so that we do not expect synchrotron fading (see Sect. 3).

3. HYDRODYNAMIC FLUX TUBE MODEL FOR RADIO HARPS

Already the detection of radio harps is a strong argument in favor of CR propagation with v_a : CRs leaving the source have individual trajectories that are preferentially aligned with the magnetic flux tube. As NTFs lay mostly perpendicular to the Galactic plane, the synchrotron radiation should be beamed away from the Galactic plane and undetectable for us. Thus, to explain the NTF detection some mechanism is needed that effectively scatters CRs such that their beamed radiation is observable with radio telescopes. A likely possibility is pitch-angle scattering by gyroresonant Alfvén waves. CRs moving along a flux-tube can excite these Alfvén waves via the gyroresonant instability, which leads to CR streaming close to the Alfvén speed, v_a (see Sect. 1).

We model CR electron propagation inside NTFs with the following numerical setup: we assume self-similar evolution of the individual filaments in a given harp and that the observation samples the evolution of an

archetypical NTF at different times. Within a propagation model, this allows us to conduct a single simulation for all filaments. Filaments of different lengths correspond to different simulation times: longer filaments correspond to later times with a broadened CR distribution.

We assume an Alfvén speed of $v_a = 40 \text{ km s}^{-1}$ and use ISM parameters as detailed in Sect. 2. The simulation domain is aligned with the magnetic flux tube, which is assumed to be straight and to have a constant cross section πR^2 during the simulation. The CR electrons are initialised by injecting $E_{\text{CR}} = 5 \times 10^{42} \text{ erg}$ into a Gaussian with width 0.05 pc to model CR injection at the bow shock of a massive star or pulsar.

1. The *diffusion* model assumes that the CRs diffuse along the magnetic flux tubes with a constant coefficient $\kappa = 3 \times 10^{25} \text{ cm}^2 \text{ s}^{-1}$, which was chosen to match NTF sizes with a diffusion length scale $l = \sqrt{2\kappa t}$ and $t = 30 \text{ kyr}$.¹ We include Alfvén wave cooling of CRs (see Pfrommer et al. 2017).
2. The *streaming + diffusion* model uses the more accurate description for CR transport of Thomas & Pfrommer (2019), which evolves the CR energy and momentum density. In addition, the energy contained in gyroresonant Alfvén waves is evolved and coupled to CRs using quasi-linear theory of CR transport. We only consider non-linear Landau damping of Alfvén waves (see Thomas & Pfrommer 2019). The initial CR energy flux is chosen so that CRs stream with v_a .

The *streaming + diffusion* model includes details of the microphysical interaction of CRs and Alfvén waves that are absent in the pure *diffusion* model which is unable to model CR streaming. In comparison to the *diffusion* model, where the diffusion coefficient κ is constant, the diffusion coefficient in the *streaming + diffusion* model is calculated based on the local strength of Alfvén waves. We solve the equations of Thomas & Pfrommer (2019) using a finite volume method (Thomas et al. in prep) in the moving mesh code AREPO (Springel 2010) for both models (in the *diffusion* model κ is constant). We use a one-dimensional grid with 4096 cells, a grid spacing of $\Delta x = 4 \times 10^{-3} \text{ pc}$, and outflowing boundary conditions. A reduced speed of light $\tilde{c} = 1000 \text{ km s}^{-1}$ is used and we confirmed that the presented results are robust for changes of \tilde{c} .

¹ In the *diffusion* model, only the combination κt is constrained by the diffusion length; for simplicity, we use the time scale of the *streaming + diffusion* model.

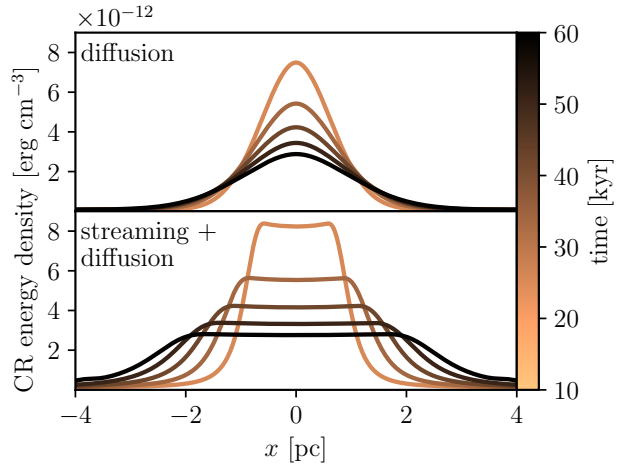


Figure 4. Evolution of the energy densities of CR electrons for the two propagation models over the course of 60 kyr.

We present the evolution of the CR electron energy density in Fig. 4. The result for the *diffusion* model resembles the typical evolution of a diffusion process: the initial Gaussian approximately maintains its shape while increasing its physical extent. The deviations from a pure diffusion profile are caused by CR energy losses due to Alfvén-wave cooling.

Including the interactions between CRs and Alfvén waves allows CRs to enter the streaming mode of CR transport. Therein the two wings of the Gaussian are traveling at speeds of $\sim \pm v_a$ in opposite directions. In between the two wings the CRs are rarefied causing the development of a plateau of almost constant energy density. At later times, the CRs are unable to maintain a high level of energy contained in Alfvén waves. As a result, CRs get less frequently scattered and enter the diffusive regime of CR transport.

4. COMPARISON TO OBSERVATIONS

We extract radio brightness profiles of the MeerKAT filaments (Heywood et al. 2019) by taking cuts along the individual filaments of the harp G359.47+0.12, shown in Fig. 2 on the right. We use one segment for the three brightest filaments, respectively, and four segments for the faintest filament to trace its curvature. In Fig. 5, we compare this to our simulations by scaling the simulated CR energy density with a constant factor to match the observed radio flux. This factor is chosen so that the brightness in the first filament approximately agrees with the scaled simulated profiles. To match the brightness of the third and fourth filament in the *streaming + diffusion* model, we had to increase the scaling by 25% and 40%, respectively. For the *diffusion* model, we need to increase these factors by 50%. The displayed

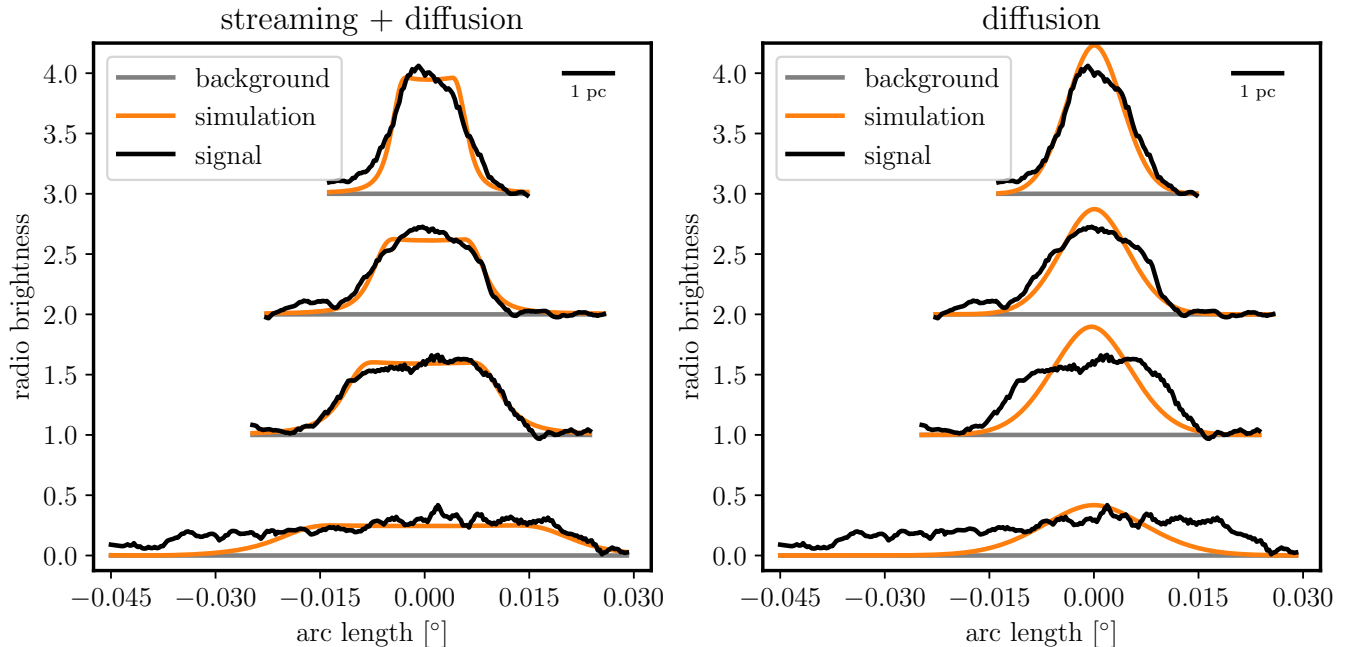


Figure 5. Comparison between the observed radio emission from the radio harp G359.47+0.12 (extracted from Heywood et al. 2019) and the simulated profiles. The simulated profiles are displayed at times 16.4, 25.6, 36.9 and 71.8 kyr (top to bottom) after CR injection. The filaments each have an offset of 1 in the y -direction. We convert physical distances in the simulation to angular sizes assuming a distance of 8.2 kpc to the CMZ. The *streaming + diffusion* model matches the MeerKAT radio data significantly better than the *diffusion* model.

background noise level is calculated by averaging the diffusive background excluding resolved and bright sources.

Only the *streaming + diffusion* model agrees with the observed profiles while the *diffusion* model is unable to reproduce the central flat emission at late times because the diffusion profile never loses its central maximum. This causes a persistent overshoot in the very center and an underestimation of emission away so that the transition into the background is poorly modeled. The simulated Gaussian CR distribution progressively loses any steep gradients due to diffusion whereas the observations show continuously sharp transitions. Contrarily, both features can be nicely explained by including the effects of CR streaming as done in the *streaming + diffusion* model. Therein, the flat emission naturally corresponds to the plateau of the rarefying CR energy density while the expanding fronts of the CR distribution follow the steep transition of the radio emission.

There are no primary beam corrections applied to the four pointings that make up the MeerKAT mosaic (Heywood et al. 2019). While this precludes accurate photometry of the large-scale emission, the small-scale radio-harp profiles should mostly be unaffected. We note that the image of G359.47+0.12 shows a circularly shaped area with reduced flux levels of filaments and background emission, which is centered just outside the image in the lower right part of Fig. 2. This reduced

flux might be an artefact of the lacking primary beam corrections during imaging (Heywood et al. 2019) and could explain the asymmetric shape of the older synchrotron filaments in Fig. 5. If correct, the agreement of the *streaming + diffusion* model with the observation may improve even more after primary beam corrections and the *diffusion* model will become worse, strengthening our finding.

We attempted to apply the same analysis to the harp G359.85+0.39. However, its filaments appear to be overlapping in projection. Whether the overlap is caused by the projection of individual spatially separated or of braided flux tubes that divert away from the central bright emission is not obvious. This ambiguity precludes a simple emission modeling of the complex flux-tube structure. However, the morphological similarity of both harps, which exhibit the shape of an inverted bell curve, strongly suggests that CR streaming is responsible for the emission structure in both cases.

We predict a massive star or pulsar at the tip of each radio harp and encourage observers to search for them.

5. CONCLUSIONS

Here, we presented a model that explains the morphological appearance of the new phenomenon of radio harps observed within the bipolar outflows by MeerKAT. A careful modeling of two competing CR

transport schemes (pure CR diffusion and a combination of CR streaming and diffusion in the self-confinement picture) demonstrates that only the CR *streaming* model is able to match the detailed brightness distributions of the individual NTFs of the harp G359.47+0.12. The intermittency of the harp emission either reveals details of the magnetic field structure or about the magnetic reconnection processes at the interface of the shocked stellar (or pulsar) wind with the surrounding interstellar magnetic field. We hope that future high-resolution observations shed light on this, further enable

us to disentangle the possibly three-dimensional structure of the other harp G359.85+0.39, and detect even more examples of this phenomenon. This will consolidate our conclusions regarding the CR streaming to be the relevant propagation mode for CRs at GeV energies.

TT and CP acknowledge support by the European Research Council under ERC-CoG grant CRAGSMAN-646955. This research was supported in part by the National Science Foundation under Grant No. NSF PHY-1748958.

REFERENCES

- Barkov, M. V., & Lyutikov, M. 2019, MNRAS, 489, L28
- Barkov, M. V., Lyutikov, M., & Khangulyan, D. 2019, MNRAS, 484, 4760
- Benaglia, P., Romero, G. E., Martí, J., Peri, C. S., & Araudo, A. T. 2010, A&A, 517, L10
- Bicknell, G. V., & Li, J. 2001, ApJL, 548, L69
- Blasi, P., Amato, E., & Serpico, P. D. 2012, PhRvL, 109, 061101
- Bykov, A. M., Amato, E., Petrov, A. E., Krassilchtchikov, A. M., & Levenfish, K. P. 2017, SSRv, 207, 235
- Caprioli, D., & Spitkovsky, A. 2014, ApJ, 783, 91
- Dahlburg, R. B., Einaudi, G., LaRosa, T. N., & Shore, S. N. 2002, ApJ, 568, 220
- del Valle, M. V., & Pohl, M. 2018, ApJ, 864, 19
- Heywood, I., Camilo, F., Cotton, W. D., et al. 2019, Nature, 573, 235
- Kulsrud, R., & Pearce, W. P. 1969, ApJ, 156, 445
- Lang, C. C., Anantharamaiah, K. R., Kassim, N. E., & Lazio, T. J. W. 1999, ApJL, 521, L41
- LaRosa, T. N., Lazio, T. J. W., & Kassim, N. E. 2001, ApJ, 563, 163
- Law, C. J., Yusef-Zadeh, F., & Cotton, W. D. 2008, ApJS, 177, 515
- Lesch, H., & Reich, W. 1992, A&A, 264, 493
- Linden, T., Hooper, D., & Yusef-Zadeh, F. 2011, ApJ, 741, 95
- Malkov, M. A. 2017, PhRvD, 95, 023007
- Nord, M. E., Lazio, T. J. W., Kassim, N. E., et al. 2004, AJ, 128, 1646
- Pfrommer, C., Pakmor, R., Schaal, K., Simpson, C. M., & Springel, V. 2017, MNRAS, 465, 4500
- Rosner, R., & Bodo, G. 1996, ApJL, 470, L49
- Shore, S. N., & LaRosa, T. N. 1999, ApJ, 521, 587
- Springel, V. 2010, MNRAS, 401, 791
- Thomas, T., & Pfrommer, C. 2019, MNRAS, 485, 2977
- Xu, R., Spitkovsky, A., & Caprioli, D. 2019, arXiv e-prints, arXiv:1908.07890
- Yan, H., & Lazarian, A. 2011, ApJ, 731, 35
- Yusef-Zadeh, F. 2003, ApJ, 598, 325
- Yusef-Zadeh, F., Hewitt, J. W., & Cotton, W. 2004, ApJS, 155, 421
- Yusef-Zadeh, F., & Wardle, M. 2019, MNRAS, 490, L1